Article

Ligand Characterization and DNA Intercalation of Ru(II) Polypyridyl Complexes: A Local Vibrational Mode Study

Published as part of The Journal of Physical Chemistry A virtual special issue "Gustavo Scuseria Festschrift".

Hunter La Force, Marek Freindorf, and Elfi Kraka*

Read Online

ACCESS | Metrics & More | Article Recommendations | Supporting Information

ABSTRACT: We investigated in this work ruthenium-ligand bonding across the RuN framework in 12 Ru(II) polypyridyl complexes in the gas phase and solution for both singlet and triplet states, in addition to their affinity for DNA binding through $\pi-\pi$ stacking interactions with DNA nucleobases. As a tool to assess the intrinsic strength of the ruthenium-ligand bonds, we determined local vibrational force constants via our local vibrational mode analysis software. We introduced a novel local force constant that directly accounts for the intrinsic strength of the $\pi-\pi$ stacking interaction between DNA and the intercalated Ru(II) complex. According to our findings, $[Ru(phen)_2(dppz)]^{2+}$ and $[Ru-(phen)_2(11\text{-}CN\text{-}dppz)]^{2+}$ provide an intriguing trade-off between photoinduced complex excitation and the strength of the subsequent

$\pi-\pi$ stacking interaction with DNA. $[Ru(phen)_2(dppz)]^{2+}$ displays a small singlet−triplet splitting and a strong $\pi-\pi$ stacking interaction in its singlet state, suggesting a favorable photoexcitation but potentially weaker interaction with DNA in the excited state. Conversely, $[Ru(phen)_2(11\text{-}CN\text{-}dppz)]^{2+}$ exhibits a larger singlet−triplet splitting and a stronger $\pi-\pi$ stacking interaction with DNA in its triplet state, indicating a less favorable photoinduced transition but a stronger interaction with DNA postexcitation. We hope our study will inspire future experimental and computational work aimed at the design of novel Ru-polypyridyl drug candidates and that our new quantitative measure of $\pi-\pi$ stacking interactions in DNA will find a general application in the field.
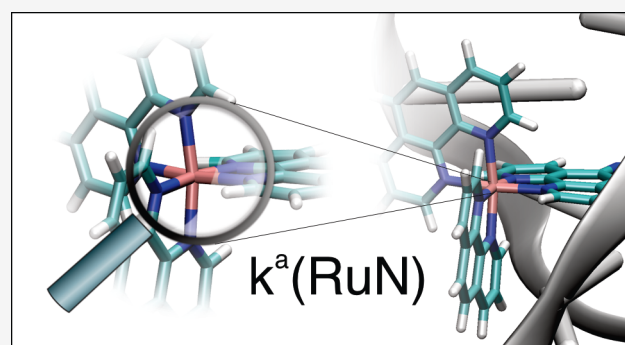
INTRODUCTION

Organometallic complexes have attracted attention over the past decades as potential anticancer drugs,[1,2] with the DNA-targeting cisplatin being one of the most prominent representatives.[3,4] However, over time, several clinical problems arose with cisplatin and other platinum drugs, including bacterial resistance, a limited spectrum of activity, and considerable side effects.[5] This spurred efforts to design new generations of organometallic anticancer complexes to overcome these deficiencies. Ruthenium complexes have displayed significant potential for their diverse chemical properties.[6] Prior ruthenium drugs that have pioneered these endeavors include NAMI-A,[7,8] NKP1339,[9] and KP1019[10] seeing phase I of clinical trials, and TLD1433[11] seeing phase II of clinical trials in treating colorectal cancers. Modern contenders include arene ruthenium drugs such as RM175, RAPTA-C, and RAPTA-T complexes.[12−14]

Ruthenium(II) polypyridyl complexes belonging to the family of luminescent transition metal complexes have garnered attention for their tunable photochemical and photophysical properties.[15] Upon photoexcitation, these complexes undergo metal-to-ligand charge transfer (MLCT) with an electron shifting from a metal *d* orbital to a ligand

orbital, forming an excited state with distinct electronic properties.[16] This excited state can, in turn, engage in intersystem crossing to populate a long-lived triplet state. In the presence of molecular oxygen, this triplet state can catalyze the generation of reactive oxygen species (ROS) such as singlet oxygen or superoxide radicals.[17] The highly reactive ROS have been instrumental in inducing cytotoxic effects, particularly within cancer cells, making Ru(II) polypyridyl complexes promising agents for photodynamic therapy in hypoxic tumor environments.[18−21] Concurrently, MLCT also facilitates phosphorescence upon relaxation to the ground state, a property valuable for imaging applications.[22,23]

Onset by the discovery that $[Ru(bpy)_2(dppz)]^{2+}$ (bpy = 2,2′-bipyridine, dppz = dipyrido[3,2-*a*:2′,3′-*c*]phenazine) binds to DNA with high affinity with an accompanying
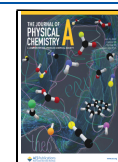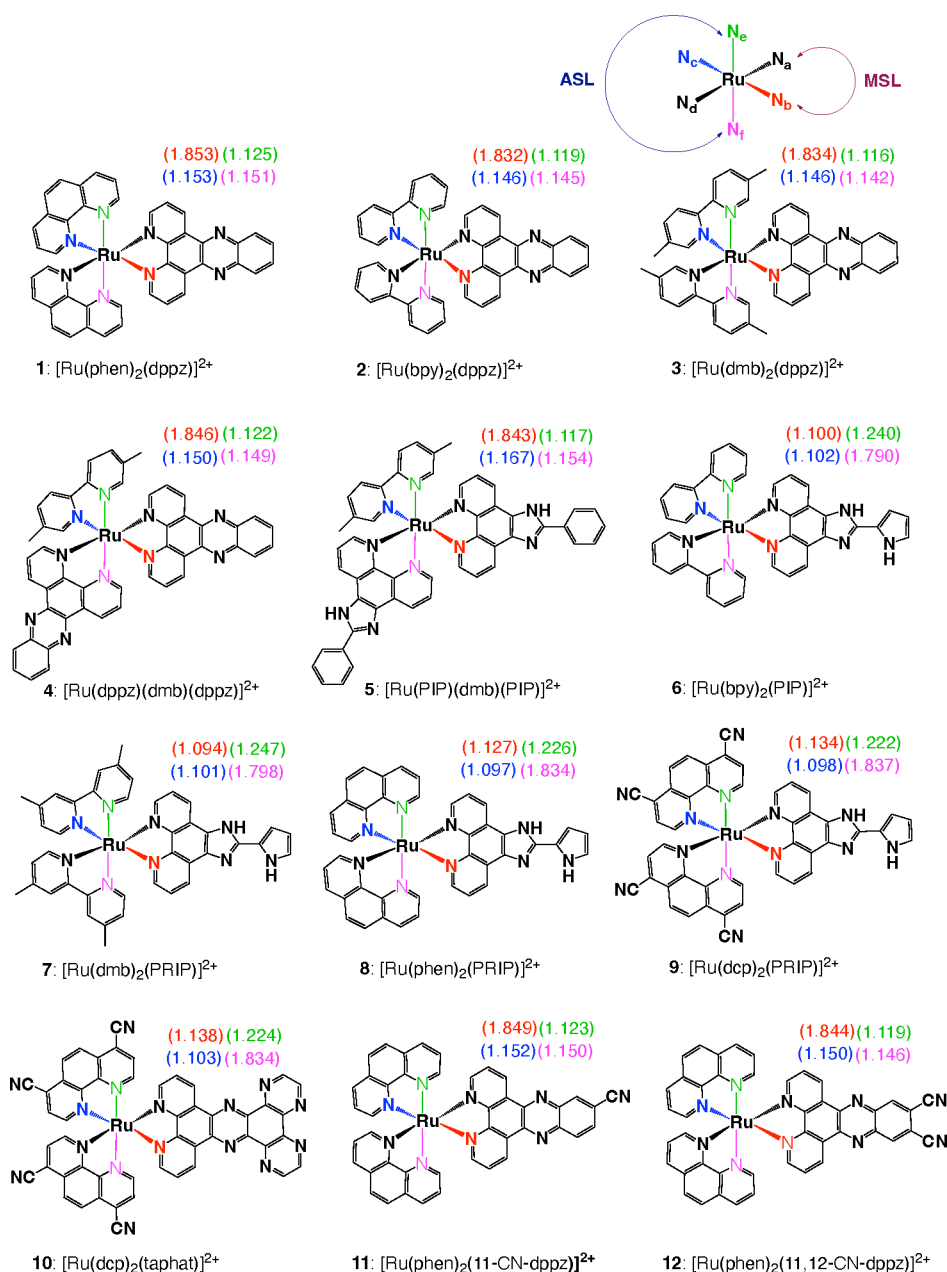
Figure 1. Overview of the 12 Ru(II) polypyridyl complexes studied. The local mode force constants of RuN$_b$ bonds (red), RuN$_c$ bonds (blue), RuN$_e$ bonds (green), and RuN$_f$ bonds (magenta) are listed for each complex in the series for the singlet gas-phase geometries using a PBE0/cc-pVTZ/SDD(Ru) level of theory (mdyn/Å), where the main stacking ligand (MSL) is annotated in dark red and the ancillary stacking ligands (ASL) are annotated in dark blue.

increase in MLCT luminescence, the so-called DNA *light switch* effect,[24] a variety of ruthenium(II) polypyridyl complexes with different intercalating ligands have been developed as high-affinity DNA binders.[25,26] In order to fine-tune these ruthenium(II) polypyridyl complexes via systematic ligand modifications, one must analyze Ru-ligand bonding and the strength of the bonds with a qualified measure of bond strength. Thus, a reliable measure of the strength of DNA intercalation is needed in the case of Ru(II) polypyridyl complexes acting as π−π stacking agents.[27,28] Such a measure is provided by the local vibrational stretching force constants derived from our Local Vibrational Mode Theory,[29,30] which we've applied in this study to a set of 12 representative ruthenium(II) polypyridyl complexes shown in Figure 1.[27,31,32]

Complex **1** was obtained from the PDB structure of intercalated Ru(II)−DNA complex (PDB: 3U38).[33] Complexes **2−5** were motivated by the prior work of Elgar et al.[31] and were selected to assess how changes in the ASL, with identical MSLs, cause changes in the strengths of the RuN ligand bonds. Ru(phen)$_2$(dppz)]$^{2+}$ (phen = 1,10-phenanthroline) (**1**), contains a (dppz) MSL and a (phen)$_2$ ASL, while [Ru(bpy)$_2$(dppz)]$^{2+}$ (**2**) and [Ru(dmb)$_2$(dppz)]$^{2+}$ (**3**) (dmb = 5,5′-dimethyl-2,2′ bipyridine) also display a (dppz) MSL with a (bpy)$_2$ ASL or (dmb)$_2$ ASL, respectively. [Ru(dppz)(dmb)-(dppz)]$^{2+}$ (**4**) again displays a (dppz) MSL and an ASL composed of (dppz) and (dmb). [Ru(PIP)(dmb)(PIP)]$^{2+}$ (**5**) (PIP = 2-phenyl-imidazo-[4,5-*f*][1,10]phenanthroline) displays a (PIP) MSL and an ASL similarly composed of (PIP)
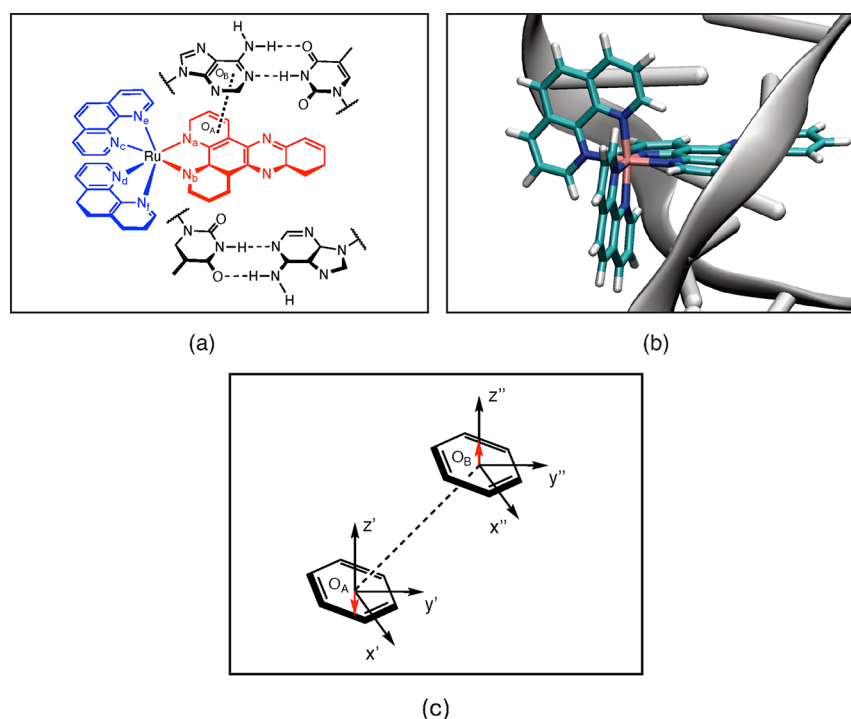
Figure 2. Series of images depicting (a) MSL (red) and ASL (blue) along with the interaction of interest for this study, as depicted by the noncovalent interaction spanning one of the rings on MSL (O_A) and the six-membered ring of the nucleobase Adenine (O_B), (b) visualization of the QM/MM system with the QM region (the ligand) depicted in color and the MM region (the DNA strand) depicted in gray, and (c) definition of the S_z local mode spanning a benzene ring A and a benzene ring B. O_A is the geometric center of the monomer A, where O_B and $x'y'z'$ define a standard orientation of ring B from the mean ring plane.[53] $x''y''z''$ are the projected coordinates $x'y'z'$ from O_A to O_B. Reprinted (adapted) with permission from Juliana J. Antonio and Elfi Kraka *Biochemistry* 2023, *62*, 2325−2337. Copyright 2024 American Chemical Society.

and (dmb). The inclusion of **5**, in conjunction with **4**, was provided to demonstrate how parallel substitutions in the MSL and ASL correspond to changes in the strengths of the RuN bonds.

Complexes **6**−**10** were motivated by the prior work of Miao et al.[32] $[Ru(bpy)_2(PIP)]^{2+}$ (**6**) displays a (PIP) MSL and an ASL composed of $(bpy)_2$, mimicking the substitution pattern of **2**. $[Ru(dmb)_2(PRIP)]^{2+}$ (**7**), $[Ru(phen)_2(PRIP)]^{2+}$ (**8**), and $[Ru(dcp)_2(PRIP)]^{2+}$ (**9**) (dcp = 4,7-dicarbonitrile-1,10-phenanthroline) were chosen to simultaneously compare how modifying ASLs with unique (PRIP) MSLs changes the bond strengths of RuN ligand bonds. $[Ru(dcp)_2(taphat)]^{2+}$ (**10**) (taphat = 1,4,5,8-tetraazaphenanthrene-1,4,5,8,9,12-hexaazatriphenylene) was employed in our study as an example what happens compared to **9** when the MSL is changed rather than the ASL and additionally showcasing the effects of extended π-conjugated MSLs on the bond strengths of the central RuN bonds.

Finally, we included two model complexes, $Ru(phen)_2(11-CN-dppz)]^{2+}$ (**11**) [(11-CN-dppz = 11-cyano-dipyrido[3,2-*a*:2′,3′-*c*]phenazine) and $[Ru(phen)_2(11,12-CN-dppz)]^{2+}$ (**12**) (11,12-CN-dppz = 11,12-dicyano-dipyrido[3,2-*a*:2′,3′-*c*]-phenazine), that we designed to directly compare the effects of single and double terminal nitrile substitution on the MSL of **1**. This inclusion was inspired by prior work of McQuaid et al.,[27] which proposes terminal nitrile substitution positively impacts the π−π stacking interactions of Ru(II) DNA-intercalators with the nucleobase Adenine.

COMPUTATIONAL METHODS

All geometry optimizations and frequency calculations were conducted using DFT[34] using a PBE0/cc-pVTZ level of theory.[35,36] The PBE0 hybrid functional was selected based on previous studies, indicating its superior agreement with experimental results for ruthenium-methylimidazole complexes,[37,38] our prior work with ruthenium complexes,[39,40] and its suitable performance for the description of organometallic compounds.[41−43] To account for relativistic effects observed with second-row transition metals, the Stuttgart−Dresden effective core potential (SDD) was used.[44,45] SDD is a quasi-relativistic *ab initio* pseudo-potential that substitutes the $M(Z-28)^+$ core orbitals with the more optimized GTO valence basis set that includes the corresponding spin−orbit coupling operator.[45] For all triplet state calculations, unrestricted DFT was employed.[46] To model the complexes in solution, a polarizable continuum model (PCM) was used.[47] An Ultra-Fine integration grid was used in all DFT calculations.[48]

A hybrid quantum chemistry/molecular mechanics (QM/MM) methodology[49−52] was used to model the nonbonded interactions involved in the base−pair stacking of Ru(II) polypyridyl complexes **1**, **2**, **3**, and **11**, representing different MSL and ASL scenarios, within AT/TA gaps of DNA.

These calculations were initiated from the X-ray diffraction structure of $\Lambda-[Ru(phen)_2dppz]^{2+}$ with oligonucleotides (PDB entry: 3U38).[33] Figure 2 illustrates the primary nonbonded interaction investigated in this study, focusing on one of the ligand rings stacking against the adjacent six−membered ring of an Adenine nucleobase. The Ru(II) complexes were treated with quantum mechanical methods, while the DNA strand was treated with molecular mechanics.

Table 1. Parameters of RuN_b and RuN_c Bonds for the Singlet and Triplet Electronic States in the Gas Phase[a]

	singlet					triplet				
complex	q_n	k^a	BSO n	ρ_b	H_b	q_n	k^a	BSO n	ρ_b	H_b
					RuN_b bond					
1	2.905	1.853	0.945	0.645	−0.124	2.900	1.856	0.946	0.655	−0.169
2	2.909	1.832	0.941	0.656	−0.129	2.903	1.836	0.942	0.653	−0.176
3	2.908	1.834	0.941	0.659	−0.131	2.872	1.918	0.958	0.772	−0.258
4	2.906	1.846	0.944	0.642	−0.122	2.905	1.846	0.944	0.654	−0.167
5	2.905	1.843	0.943	0.651	−0.124	2.894	1.861	0.947	0.833	−0.295
6	3.050	1.100	0.772	0.665	−0.140	3.054	1.079	0.766	0.658	−0.171
7	3.055	1.094	0.770	0.665	−0.140	3.062	1.058	0.761	0.656	−0.170
8	3.085	1.127	0.779	0.648	−0.133	3.069	1.118	0.777	0.667	−0.185
9	3.081	1.134	0.781	0.652	−0.134	3.084	1.127	0.779	0.670	−0.179
10	3.081	1.138	0.782	0.651	−0.132	3.079	1.134	0.781	0.670	−0.180
11	2.906	1.849	0.944	0.643	−0.123	2.867	1.922	0.959	0.781	−0.263
12	2.907	1.844	0.943	0.642	−0.122	2.869	1.945	0.963	0.775	−0.259
					RuN_c bond					
1	6.550	1.153	0.786	0.657	−0.170	6.577	1.115	0.776	0.653	−0.167
2	6.553	1.146	0.784	0.668	−0.176	6.580	1.109	0.775	0.757	−0.245
3	6.552	1.146	0.784	0.652	−0.166	6.525	1.180	0.793	0.654	−0.175
4	6.550	1.150	0.786	0.657	−0.170	6.550	1.150	0.786	0.670	−0.177
5	6.616	1.167	0.790	0.656	−0.164	6.595	1.213	0.802	0.632	−0.160
6	4.351	1.102	0.773	0.653	−0.118	4.355	1.079	0.766	0.671	−0.177
7	4.352	1.101	0.772	0.648	−0.114	4.359	1.065	0.763	0.669	−0.177
8	4.388	1.097	0.771	0.638	−0.109	4.356	1.003	0.745	0.744	−0.237
9	4.382	1.098	0.772	0.641	−0.114	4.383	1.089	0.769	0.663	−0.173
10	4.382	1.103	0.773	0.642	−0.114	4.380	1.099	0.772	0.654	−0.168
11	6.549	1.152	0.786	0.658	−0.171	6.520	1.179	0.793	0.632	−0.162
12	6.549	1.150	0.786	0.657	−0.171	6.523	1.191	0.796	0.634	−0.164

[a]Bond length (Å), local mode force constant (mdyn/A), bond strength order BSO n, electron density ρ_b (e/Å^3) and energy density at bond critical point H_b (Har/Å^3).

Metal force field parameters were generated using Metal Center Parameter Builder (MCPB),[54] and the entire molecular system was neutralized with 18 Na^+ ions and solvated with TIP3P water molecules within a 16 Å radius of the metal center.[55] Initial minimization at the MM level was conducted using Amber,[56] followed by QM/MM geometry optimization using ONIOM with electronic embedding,[57] employing the PBE0/cc-pVTZ/SDD(Ru)/Amber level of theory for both singlet and triplet electronic states. After geometry optimization, QM/MM frequency calculations were performed, ensuring the absence of imaginary modes. The nonbonded interaction between the complex and the nucleobase was evaluated using the optimized QM/MM geometry with the LModeA program to analyze the interaction between the complex's MSL rings and the nucleobase. We have selected those aromatic rings, which were separated by a distance smaller than 3.6 Å.[28] The nonbonded interaction was defined as an S_z local mode (see Figure 2), representing an intramonomer stretching mode from one of the ligands rings to Adenine's six-membered ring in the z-direction, as this has previously been proposed to serve as a major component for the nonbonded interaction for these complexes.[27] The initial geometries of the other three ligands in DNA (**2**, **3**, and **11**) were obtained by manually modifying Λ-[Ru(phen)$_2$dppz]$^{2+}$ (**1**), and QM/MM calculations were performed using the same protocol.

The local vibrational mode analysis (LMA), originally developed by Konkoli and Cremer, has become a versatile tool for extracting important chemical information from vibrational spectroscopy, often hidden due to the delocalized nature of normal vibrational modes in polyatomic molecules.[58] While leading to a new way to analyze vibrational spectra, as shown in the composition of normal mode (CNM) analysis,[59] LMA has led to a new quantitative measure of chemical bond strength and nonbonded interactions based on local vibrational mode force constants (k^a).[60] The underlying theory and a comprehensive overview of LMA applications can be found in two recent review articles.[29,30] Rather than directly comparing values of local force constants, it is routine to associate a bond strength order (BSO n) for a series of compounds. This relationship can be described by a generalized Badger rule, as shown from the work of Kraka et al.:[61] BSO $n = A(k^a)^B$. The constants A and B can be determined using two reference compounds with known k^a and the requirement that for a zero k^a the corresponding BSO n value is zero. For this work, using RuH and RuO as reference molecules, the values of those constants were determined to be $A = 0.7441$ and $B = 0.3879$, based on scaled Mayer bond orders[62] (1.0 for the RuH bond and 1.5803 for the RuO bond) and local mode force constants (2.143 mdyn/Å for RuH and 6.978 mdyn/Å for RuO). These calculations were performed using a PBE0/cc-pVTZ/SDD-(Ru) level of theory.[39,40] The covalent nature of the RuN bonds was evaluated using the Cremer−Kraka criterion,[63,64] which analyzes the energy density H_b at the bond critical point r_b along the electron density path connecting two atoms involved in the chemical bond in question, as defined in Bader's QTAIM (quantum theory of atoms in molecules) model.[65,66] A negative value of H_b indicates a more covalent character of the chemical bond or interaction, whereas a positive value reflects a more electrostatic character.
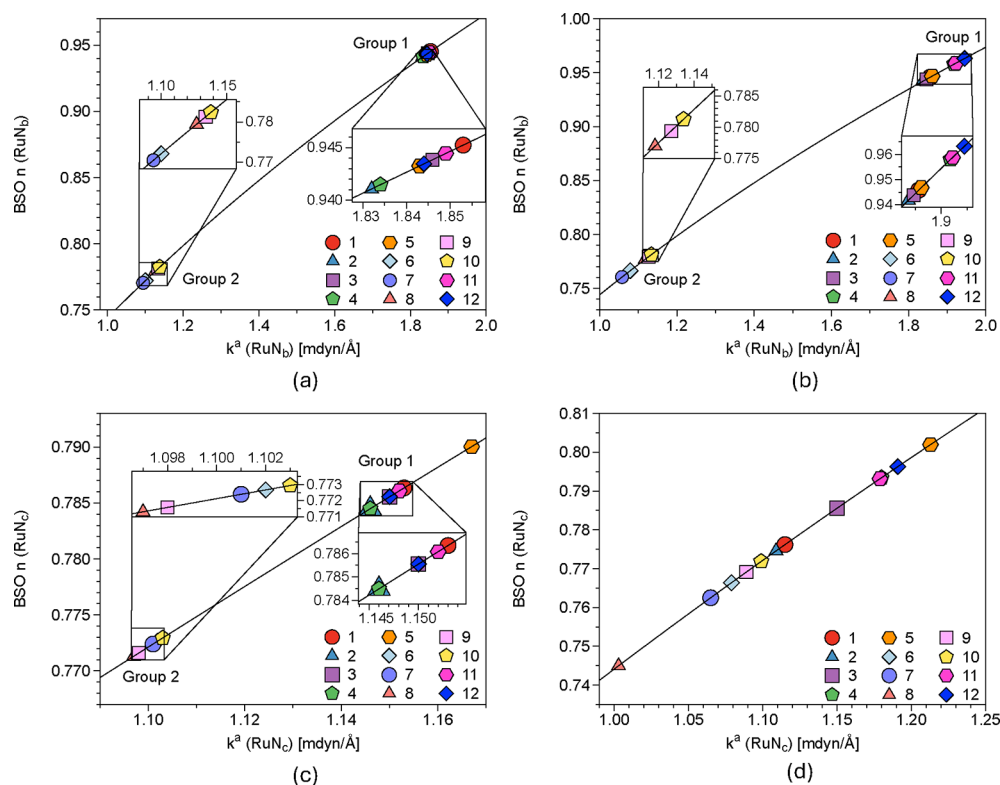
Figure 3. BSO n as a function of local mode force constant k^a for RuN bonds in the gas phase: (a) RuN_b singlet state; (b) RuN_b triplet state; (c) RuN_c singlet state; (d) RuN_c triplet state.

RESULTS AND DISCUSSION

This section summarizes the key findings of this study. First, results for RuN_b and RuN_c bonds and RuN_e and RuN_f bonds in their singlet and triplet states are discussed in the gas phase. Then, the results for these bonds are displayed in solution. Finally, QM/MM DNA intercalation results are presented for complexes **1**, **2**, **3**, and **11**. As the results for RuN_a and RuN_d are quite similar to those for RuN_b and RuN_c, we summarize this data in the Supporting Information. NBO charges for Ru and $N_a - N_f$ atoms can be found in the Supporting Information.

RuN_b and RuN_c Bonds in the Gas Phase. The gas phase geometries of the complexes were analyzed by using LMA parameters and QTAIM parameters for the RuN_b and RuN_c bonds. Table 1 shows the bond lengths, the local mode force constants, the BSO n values, the electron density, and the energy density at a bond critical point for RuN_b and RuN_c bonds in the singlet and triplet electronic states in the gas phase. The bonds RuN_b and RuN_c were chosen to characterize the synergistic effects of both ASL and MSL on the stability of the nonbonded interaction spanning the RuN framework. Additionally, differences in values for the bond length local mode q_n for the RuN_b and RuN_c bonds, in conjunction with their local mode force constants, distinguish the series into two groups: Group 1 exhibits larger values of k^a, indicative of stronger RuN_b along with stronger RuN_c bonds. By

comparison, Group 2 exhibits smaller values of k^a suggesting weaker but more equivalent RuN_b and RuN_c bond strengths. These local mode force constant values, in turn, supply unique BSO n values derived from the power relationship previously defined in this study.

Furthermore, these LMA parameters were interpreted in terms of the Generalized Badger Rule, and their corresponding plots are depicted in Figure 3. Figure 3a,b exhibit the local mode force constants and BSO n values for the RuN_b bond in the singlet and triplet states, respectively. It is apparent upon inspection that this bond categorizes the series into two primary groups. Group 1 comprises **1–4**, **11**, and **12**, featuring a dppz moiety in their MSL, along with **5**, which incorporates a PRIP moiety. Meanwhile, Group 2 encompasses the remaining complexes (**6–10**), all of which incorporate some variation of a PRIP scaffold in their MSL, except for **10**, which features a taphat MSL. Although **10** introduces a distinctive MSL compared to the other members of Group 2, this difference can be reconciled with the presence of the dcp ASL observed in **9**. Comparing this data to Figure 3c,d, it is evident that a trans influence can be induced from the strength of the RuN_b bond to the strength of the RuN_c bond.[72,73] Stronger RuN_b bonds are similarly associated with stronger RuN_c bonds, as observed in Group 1, while Group 2 exhibits weaker but more similar RuN_b and RuN_c bond strengths. This underscores the impact of the choice of MSL on the electronic structure of the complex, with planar fused—ring systems rich in π electrons promoting a stronger RuN_b bond, thereby better facilitating MLCT. Furthermore, Figure 3d reveals a slight deviation from this pattern, where the differences between the two groups are less pronounced but still discernible. This suggests some structural similarities in the arrangement of ASL for the triplet states of the complexes, distinct from the effects imposed by
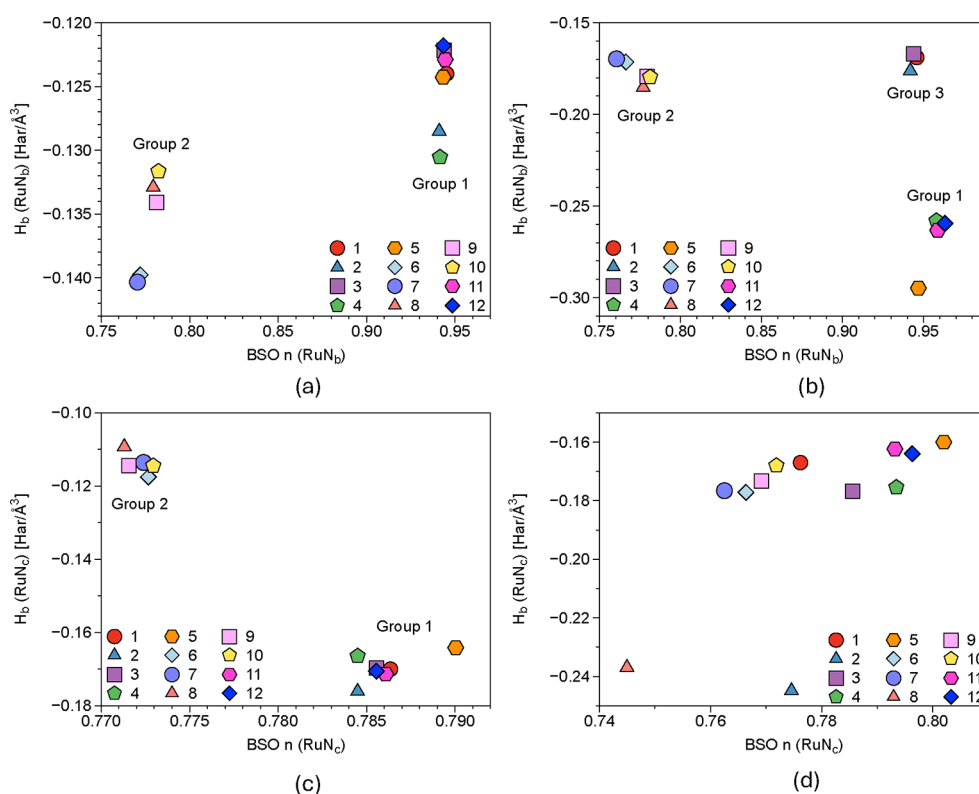
Figure 4. Relation between energy density at a bond critical point H_b and BSO n for RuN bonds in the gas phase: (a) RuN_b singlet state; (b) RuN_b triplet state; (c) RuN_c singlet state; (d) RuN_c triplet state.

Table 2. Parameters of RuN_e and RuN_f Bonds for Singlet and Triplet Electronic States in the Gas Phase[a]

complex	singlet					triplet				
	q_n	k^a	BSO n	ρ_b	H_b	q_n	k^a	BSO n	ρ_b	H_b
					RuN_e bond					
1	4.376	1.125	0.779	0.649	−0.127	4.385	1.120	0.778	0.655	−0.167
2	4.380	1.119	0.777	0.642	−0.124	4.389	1.115	0.776	0.725	−0.223
3	4.378	1.116	0.776	0.657	−0.134	4.341	1.063	0.762	0.695	−0.200
4	4.375	1.122	0.778	0.644	−0.127	4.375	1.121	0.778	0.669	−0.176
5	4.371	1.117	0.777	0.663	−0.139	4.389	1.133	0.781	0.668	−0.180
6	4.843	1.240	0.809	0.640	−0.113	4.846	1.217	0.803	0.676	−0.179
7	4.873	1.247	0.811	0.647	−0.122	4.879	1.209	0.801	0.676	−0.179
8	4.864	1.226	0.805	0.648	−0.124	4.835	1.097	0.771	0.712	−0.215
9	4.865	1.222	0.804	0.650	−0.121	4.867	1.212	0.802	0.678	−0.180
10	4.866	1.224	0.805	0.652	−0.128	4.864	1.223	0.805	0.663	−0.172
11	4.377	1.123	0.778	0.647	−0.128	4.337	1.003	0.745	0.686	−0.194
12	4.377	1.119	0.777	0.648	−0.131	4.341	1.084	0.768	0.686	−0.194
					RuN_f bond					
1	3.078	1.151	0.786	0.645	−0.127	3.082	1.149	0.785	0.655	−0.167
2	3.081	1.145	0.784	0.662	−0.135	3.086	1.143	0.784	0.724	−0.222
3	3.079	1.142	0.783	0.655	−0.131	3.071	1.181	0.794	0.695	−0.200
4	3.077	1.149	0.785	0.660	−0.134	3.076	1.147	0.785	0.651	−0.166
5	3.066	1.154	0.787	0.656	−0.135	3.097	1.186	0.795	0.710	−0.207
6	2.923	1.790	0.933	0.655	−0.135	2.925	1.750	0.924	0.673	−0.177
7	2.926	1.798	0.934	0.656	−0.136	2.931	1.732	0.921	0.670	−0.176
8	2.901	1.834	0.941	0.659	−0.137	2.882	1.389	0.845	0.702	−0.208
9	2.901	1.837	0.942	0.659	−0.135	2.903	1.807	0.936	0.673	−0.177
10	2.903	1.834	0.941	0.654	−0.135	2.901	1.837	0.942	0.662	−0.172
11	3.078	1.150	0.786	0.644	−0.126	3.067	1.148	0.785	0.685	−0.194
12	3.078	1.146	0.784	0.644	−0.124	3.069	1.196	0.798	0.686	−0.194

[a]Bond length (Å), local mode force constant (mdyn/A), bond strength order BSO n, electron density ρ_b (e/Å^3) and energy density at bond critical point H_b (Har/Å^3).
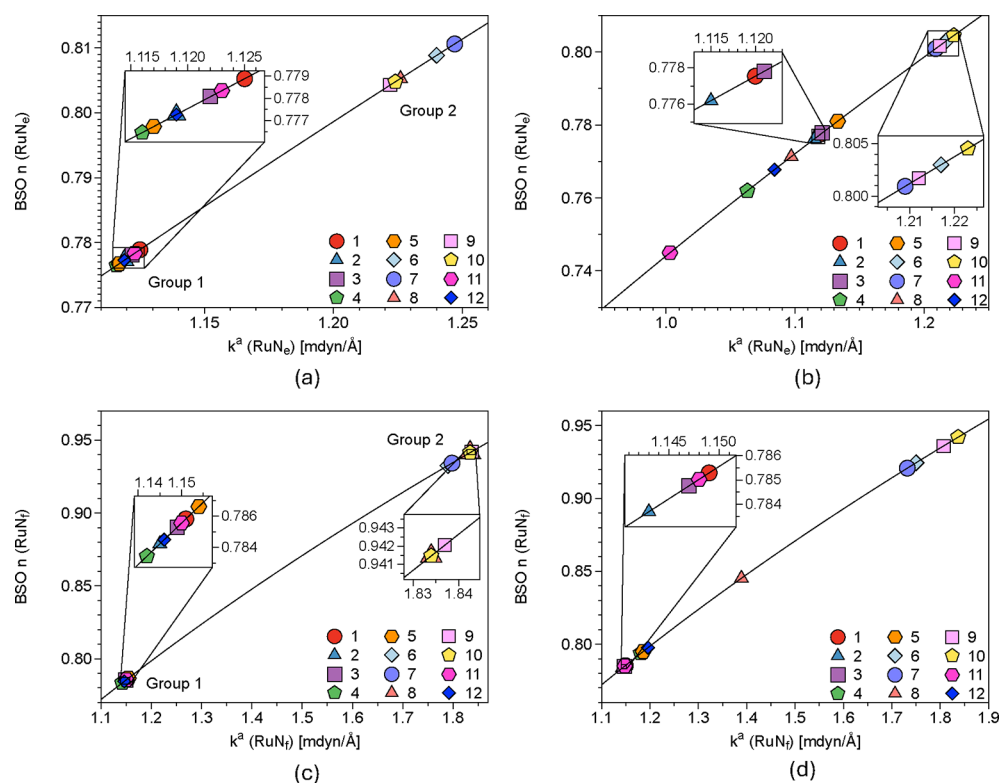
Figure 5. BSO n as a function of local mode force constant k^a for RuN bonds in the gas phase: (a) RuN$_e$ singlet state; (b) RuN$_e$ triplet state; (c) RuN$_f$ singlet state; (d) RuN$_f$ triplet state.

the MSL. Generally, these observations emphasize that the parameters in the triplet state differ from those in the singlet state, consistent with anticipated conformational disparities between different electronic excited states, where a smaller variance between local mode force constants is broadly observed.[74]

These values were subsequently compared to H_b, and their corresponding plots are illustrated in Figure 4. Figure 4a,b display the interplay between the BSO n values determined in the prior step and the associated H_b of the RuN$_b$ bond in both the singlet state and the triplet state. The trend observed from the local mode perspective is also apparent when analyzing the energy density at the bond critical point, where the RuN$_b$ bond effectively categorizes the series into Groups 1 and 2. Additionally, the triplet state further delineates a third group, Group 3, which distinguishes 1−3 from 4, 5, 11, and 12, all of which feature an unmodified dppz MSL with varying ASLs. The average BSO n value of the RuN$_b$ bond in the singlet state is 0.943 for Group 1 and 0.777 in Group 2, while its average H_b value is −0.125 Har/Å[3] for Group 1 and −0.136 Har/Å[3] in Group 2. The value of these parameters corresponds to a stronger and yet less covalent RuN$_b$ bond for Group 1, and a weaker and more covalent RuN$_b$ bond for Group 2. These average values similarly reflect the prior analysis in distinguishing Group 1 from Group 2 through their MSL. Upon examination of the RuN$_c$ bond, as depicted in Figure 4c,d, it becomes evident that the value of H_b does not uniquely differentiate the members of the series as observed for the RuN$_b$ bond. While Groups 1 and 2 are preserved for the RuN$_c$ bond in the singlet state, the reduced variance observed in the LMA parameters of the triplet state can be attributed to a similar H_b for the ASL comprising the RuN$_c$ bond. However, **2** and **8** present some exceptions to this primary grouping,

demonstrating a synergistic effect of both the MSL and the ASL on the strength of the RuN$_c$ bond, with a greater extent of energy density encompassing the RuN$_c$ bonds of both complexes. The average value of BSO n for the RuN$_c$ bond is 0.786 for Group 1 and 0.772 for Group 2, while its average H_b value is −0.170 Har/Å[3] for Group 1 and −0.114 Har/Å for Group 2. These parameters depict a stronger and more covalent RuN$_c$ bond for Group 1 and a weaker and less covalent RuN$_c$ bond for Group 2. This further justifies the trans influence observed on these bonding interactions directly affected by shifts in their electronic environments.

The characterization of LMA and QTAIM parameters of these complexes in the gas phase provides valuable insights into the trans influence exhibited by the RuN$_b$ and RuN$_c$ bonds, as well as the distinctive behavior of the RuN$_b$ bond concerning various MSLs and analogs. Altering the electronic state of these complexes notably influences the bond strength and energy density at the bond critical point, indicating structural variations in the RuN$_b$ bond attributed to changes in electronic structure. However, distinguishing notable trends in the triplet state proves more challenging for the RuN$_c$ bond, as these bonds exhibit relatively similar characteristics, regarding bond strength and covalent character.

RuN$_e$ and RuN$_f$ Bonds in the Gas Phase. In the following, we compare the relative bond strengths of these complexes' RuN$_e$ and RuN$_f$ bonds to determine the effects of differing ASL on the complexes' electronic structure. The notable parameters for these complexes can be found in Table 2, where both LMA and QTAIM parameters are listed for the RuN$_e$ and RuN$_f$ bonds. Notable differences can be observed for complexes displaying a modified dppz moiety or a PRIP scaffold in their MSL, as complexes displaying a PRIP scaffold
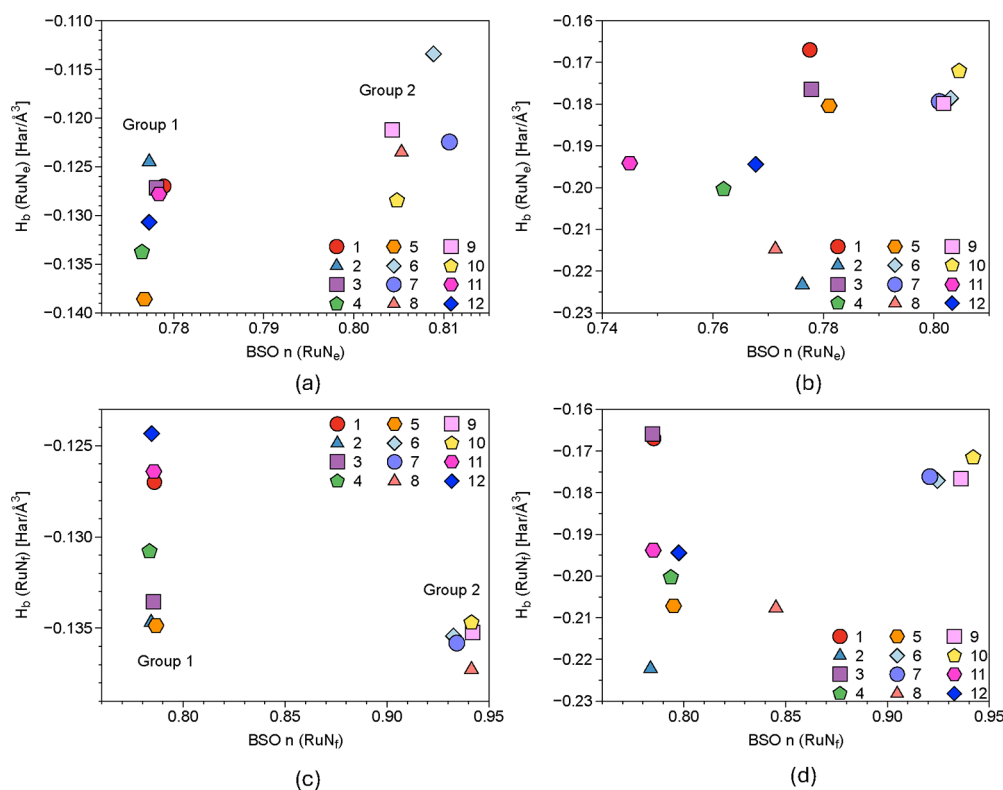
Figure 6. Relation between energy density at a bond critical point H_b and BSO n for RuN bonds in the gas phase: (a) RuN$_e$ singlet state; (b) RuN$_e$ triplet state; (c) RuN$_f$ singlet state; (d) RuN$_f$ triplet state.

present larger RuN$_f$ and RuN$_e$ strengths with smaller bond strengths seen for complexes displaying a dppz moiety.

Figure 5 displays the BSO n values for the RuN$_e$ and RuN$_f$ bonds and their functional dependence on local mode force constant k^a. Figure 5a,b display these values for the singlet and triplet states of the complexes' RuN$_e$ bonds. Groups 1 and 2 appear, yet again, in the singlet state interactions for this bond, with Group 1 displaying lower values of k^a and consequently lower values of BSO n, with Group 2 displaying higher values of k^a and higher values of BSO n. In a comparison of this trend with those previously noted for the RuN$_b$ and RuN$_c$ bonds, a higher value of $k^a(\mathrm{RuN}_b)$ is generally accompanied by a lower value of $k^a(\mathrm{RuN}_e)$ where the same can be stated for the $k^a(\mathrm{RuN}_c)$, as shown in Figure 3. This trend is obscured for the triplet state, where a mixing of the two groups is observed, and the ordering of the bond strengths of these complexes greatly varies from that of the singlet state. While this is similarly indicative of the shift in electronic properties in singlet and triplet states, this is further justified in observing Figure 5c,d, which display the strengths of the RuN$_f$ bond in the singlet and triplet states. This inverse relationship spanning the bond strengths of the RuN$_b$ and RuN$_c$ bonds with the strength of the RuN$_e$ bond can also be recognized in comparing these bonds with the RuN$_f$ bond, posing a distinct interplay in the bond strengths of RuN$_b$ and RuN$_c$ bonds with those of RuN$_e$ and RuN$_f$. This provides a fingerprint for complexes with varying ASLs and MSLs, with complexes displaying a stronger ASL interaction, displaying a weaker MSL interaction, and vice versa. While this trend is similarly recognizable in the RuN$_f$ bond of the triplet state, **8** is found nearly at the midpoint between these two groups, displaying a phen ASL common in half of the complexes observed in our study. This offers some

validity in the RuN$_f$ bond distinguishing the ASL in the series, regardless of the electronic state.

The correlations between the energy density H_b and calculated BSO n values can be shown in Figure 6. Figure 6a,b display these values for the RuN$_e$ bond in the singlet and triplet state, where Groups 1 and 2 can similarly be distinguished in the singlet state with distinct ranges of H_b values noting a greater extent of covalency in Group 1 and a lesser extent of covalency in Group 2. In a comparison of these values with those of RuN$_b$ and RuN$_c$, a more covalent RuN$_b$ bond sponsors a less covalent RuN$_e$ bond, while a more covalent RuN$_c$ bond similarly sponsors a more covalent RuN$_e$ bond.

The opposite trend can be observed in Figure 6c,d for the RuN$_f$ bond, where a more covalent RuN$_b$ bond sponsors a more covalent RuN$_f$ bond, while a more covalent RuN$_c$ bond generally sponsors a less covalent RuN$_f$ bond, as shown in Figure 4. This trend is obscured in the triplet states of these bonds, where a range of H_b can be observed for RuN$_e$ and RuN$_f$ bonds with similar bond strengths. While the average BSO n value of RuN$_e$ is 0.778 and the average value of H_b of RuN$_e$ is -0.130 Har/Å^3, similar values can be observed for the RuN$_f$ bond with the average BSO n value of 0.785 and the average value of H_b of -0.130 Har/Å^3 in the singlet state. With nearly identical values for LMA and QTAIM parameters, these bonds pose a distinct trend with RuN$_b$ and RuN$_c$ bonds, where stronger and less covalent RuN$_b$ bonds can be coupled with weaker and more covalent RuN$_e$ bonds, stronger and more covalent RuN$_c$ bonds can be coupled with weaker and less covalent RuN$_f$ bonds.

In analyzing bond strengths and H_b of RuN$_e$ and RuN$_f$ bonds comparatively with RuN$_b$ and RuN$_c$ bonds; a unique interplay of bond strength and covalency is observed. This

Table 3. Parameters of RuN$_b$ and RuN$_c$ Bonds for the Singlet and Triplet Electronic States in PCM^a

			singlet					triplet		
complex	q_n	k^a	BSO	ρ_b	H_b	q_n	k^a	BSO	ρ_b	H_b
					RuN$_b$ bond					
1	2.902	1.877	0.950	0.663	−0.172	2.897	1.876	0.950	0.661	−0.171
2	2.905	1.837	0.942	0.658	−0.169	2.900	1.840	0.943	0.656	−0.169
3	2.904	1.850	0.945	0.659	−0.170	2.899	1.850	0.945	0.657	−0.169
4	2.902	1.862	0.947	0.657	−0.169	2.897	1.861	0.947	0.656	−0.169
5	2.902	1.862	0.947	0.665	−0.174	2.892	1.909	0.956	0.724	−0.170
6	3.044	1.119	0.777	0.664	−0.173	3.029	1.125	0.779	0.622	−0.104
7	3.049	1.123	0.780	0.666	−0.174	3.053	1.092	0.771	0.668	−0.177
8	3.079	1.156	0.787	0.669	−0.176	3.065	1.128	0.780	0.666	−0.184
9	3.068	1.191	0.796	0.668	−0.178	3.053	1.230	0.806	0.664	−0.173
10	3.067	1.211	0.801	0.665	−0.174	3.065	1.212	0.802	0.659	−0.172
11	2.902	1.873	0.949	0.662	−0.171	2.888	1.907	0.956	0.714	−0.218
12	2.902	1.868	0.788	0.662	−0.171	2.895	1.889	0.787	0.677	−0.137
					RuN$_c$ bond					
1	6.543	1.160	0.788	0.660	−0.171	6.574	1.112	0.775	0.661	−0.171
2	6.547	1.144	0.784	0.677	−0.181	6.577	1.098	0.772	0.678	−0.181
3	6.546	1.151	0.786	0.677	−0.181	6.576	1.103	0.773	0.677	−0.181
4	6.544	1.155	0.787	0.675	−0.181	6.574	1.108	0.774	0.675	−0.181
5	6.604	1.176	0.792	0.674	−0.179	6.605	1.191	0.796	0.643	−0.115
6	4.344	1.123	0.778	0.675	−0.180	4.336	1.124	0.779	0.742	−0.181
7	4.346	1.130	0.780	0.673	−0.179	4.349	1.095	0.771	0.673	−0.179
8	4.381	1.125	0.779	0.658	−0.169	4.367	1.080	0.767	0.750	−0.242
9	4.368	1.142	0.783	0.669	−0.177	4.350	1.161	0.788	0.660	−0.170
10	4.368	1.164	0.789	0.670	−0.177	4.367	1.164	0.789	0.671	−0.178
11	6.540	1.163	0.789	0.661	−0.171	6.551	1.163	0.789	0.684	−0.196
12	6.539	1.160	0.788	0.661	−0.171	6.572	1.157	0.787	0.654	−0.122

^{a}Bond length (Å), local mode force constant (mdyn/A), bond strength order BSO n, electron density ρ_b (e/Å^3), and energy density at bond critical point H_b (Har/Å^3).
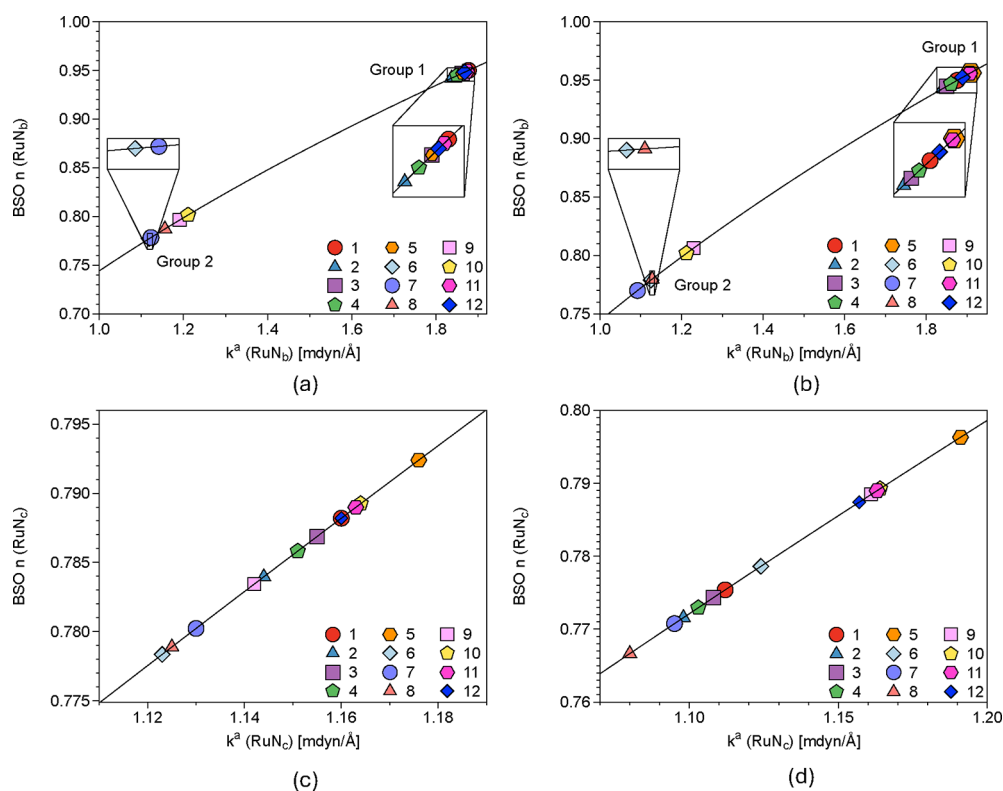

Figure 7. BSO n as a function of the local mode force constant k^a for RuN bonds in PCM: (a) RuN$_a$ singlet state; (b) RuN$_a$ triplet state; (c) RuN$_b$ singlet state; (d) RuN$_b$ triplet state.
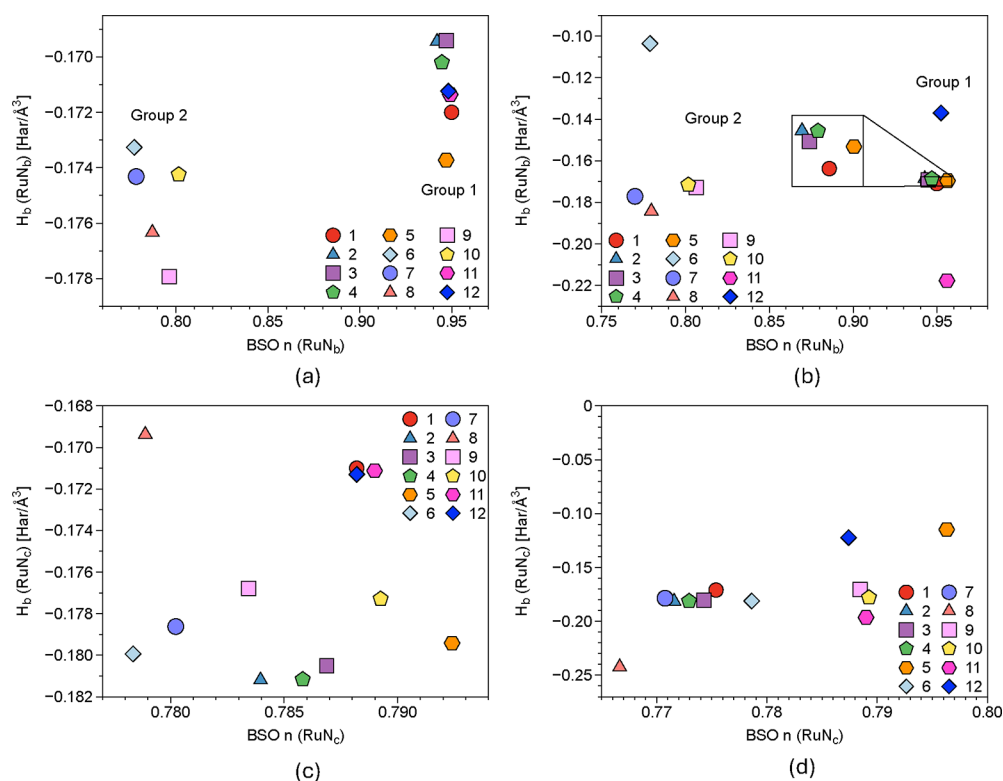
Figure 8. Relation between energy density at a bond critical point H_b and BSO n for RuN bonds in PCM: (a) RuN_b singlet state; (b) RuN_b triplet state; (c) RuN_c singlet state; (d) RuN_c triplet state.

offers a quantitative description for fine-tuning these complexes for their bond strengths with ASL and MSL, with stronger and more covalent RuN_c bonds offering weaker and less covalent RuN_f bonds, and stronger and less covalent RuN_b bonds offering weaker and more covalent RuN_e bonds. The similarity in the parameters obtained from both RuN_e and RuN_f bonds alone does not provide this description of the RuN framework; comparing RuN bonds across the scaffold using LMA, we were able to determine a synergistic effect of the strength of RuN bonds of ASL on the strength of RuN bonds of MSL.

RuN_b and RuN_c Bonds in Solution. Similarly, LMA and QTAIM parameters were examined for the complex's PCM geometries to extract intrinsic structural and electronic disparities across the series in the presence of an implicit water solvent. Table 3 presents these values, comparing the bond's electron density ρ_b with the energy density at the bond critical point H_b. LMA parameters generally reflect slightly stronger bonds, potentially influenced by solvochromatic effects on the bond strength. The RuN_b bonds show less covalent character for bonds displaying higher local mode force constants, suggesting a greater extent of electron density in the RuN framework is supplied to the MSL as opposed to the ASL, subsequently favoring DNA-stacking interactions.

As done before, the calculated LMA parameters were visualized using the Generalized Badger Rule, with the corresponding plots shown in Figure 7. Comparing these plots to those in Figure 3, the general trends for the RuN_b bonds (Figure 7a,b) persist, with Groups 1 and 2, albeit slightly enlarged as discussed earlier regarding Table 3. Complexes 9 and 10 exhibit stronger bonds in the triplet state compared to their singlet counterparts and other Group 2 members, likely due to their shared dcp ASL. However, when comparing these

findings to Figure 7c,d, the differences in bond strength observed among singlet gas phase complexes are largely absent. The previously identified groups largely overlap, suggesting similar configurations for the RuN_c bond of ASL in implicit water solvent for the singlet state. In contrast, a greater distinction emerges for the strength of the RuN_c bond in the triplet state, with 1−4 and 7 grouped, 9−12 forming another group, and 6 slightly varying from the first group. Complexess 5 and 8 serve as outliers, displaying a PRIP MSL. However, while 8 contains two phen groups in the ASL, likely sharing electron density and lowering their bond strengths, 5 contains a dmb ligand and a PRIP ancillary ligand, with the RuN_c bond exhibiting a higher strength for the less bulky dmb ligand.

These values were compared to QTAIM parameters, specifically, H_b, with their corresponding plots shown in Figure 8. Figure 8a,b depict the trends observed in prior QTAIM analyses, supporting the trends in bond strength, as determined by LMA. In the singlet state, Groups 1 and 2 are evident, with 1−5, 11, and 12 exhibiting a higher bond strength order and relatively more positive energy density values, indicating polarization of the electron density at the bond critical point of the RuN_b bond. Conversely, 6−10 display a lower bond strength order and relatively more negative energy density values, suggesting a more even electron density distribution across the bond. The triplet state exhibits slight variations in this trend, with 6, 11, and 12 acting as outliers for their respective groups, in contrast with the three groups observed in the QTAIM analysis of gas phase geometries. While 6 has less bulky bpy ASL compared to Group 2, 11 and 12 feature electron-withdrawing nitrile groups on the terminal ends of their MSLs. For 11, one nitrile group results in a greater sharing of electron density for the RuN_b bond, while for 12, two nitrile groups lead to a more uneven

Table 4. Parameters of RuN$_e$ and RuN$_f$ Bonds for the Singlet and Triplet Electronic States in PCM[a]

		singlet					triplet			
complex	q_n	k^a	BSO	ρ_b	H_b	q_n	k^a	BSO	ρ_b	H_b
					RuN$_e$ bond					
1	4.368	1.130	0.780	0.658	−0.170	4.377	1.128	0.780	0.660	−0.171
2	4.371	1.110	0.775	0.671	−0.178	4.380	1.110	0.775	0.672	−0.178
3	4.370	1.137	0.782	0.670	−0.178	4.379	1.130	0.780	0.671	−0.178
4	4.367	1.115	0.776	0.675	−0.181	4.376	1.113	0.776	0.676	−0.181
5	4.365	1.114	0.776	0.674	−0.179	4.356	1.178	0.793	0.673	−0.131
6	4.835	1.262	0.814	0.672	−0.178	4.834	1.212	0.802	0.737	−0.178
7	4.863	1.272	0.817	0.671	−0.178	4.866	1.235	0.808	0.678	−0.180
8	4.857	1.253	0.812	0.660	−0.171	4.846	1.136	0.782	0.750	−0.242
9	4.847	1.259	0.814	0.674	−0.178	4.835	1.293	0.822	0.643	−0.162
10	4.848	1.284	0.820	0.664	−0.175	4.847	1.284	0.820	0.667	−0.176
11	4.367	1.137	0.782	0.658	−0.170	4.361	1.167	0.790	0.692	−0.201
12	4.369	1.125	0.779	0.658	−0.170	4.376	1.181	0.794	0.662	−0.127
					RuN$_f$ bond					
1	3.070	1.157	0.787	0.660	−0.171	3.075	1.161	0.788	0.659	−0.170
2	3.073	1.136	0.782	0.671	−0.178	3.078	1.141	0.783	0.672	−0.178
3	3.071	1.171	0.791	0.670	−0.178	3.076	1.169	0.791	0.671	−0.178
4	3.069	1.140	0.783	0.657	−0.169	3.074	1.143	0.784	0.658	−0.170
5	3.061	1.148	0.785	0.666	−0.174	3.071	1.248	0.811	0.662	−0.124
6	2.918	1.818	0.938	0.674	−0.179	2.936	1.722	0.919	0.633	−0.109
7	2.921	1.826	0.940	0.672	−0.178	2.923	1.765	0.928	0.677	−0.180
8	2.896	1.874	0.949	0.661	−0.171	2.901	1.628	0.899	0.655	−0.177
9	2.894	1.882	0.951	0.672	−0.177	2.883	1.912	0.957	0.695	−0.193
10	2.896	1.902	0.955	0.664	−0.175	2.896	1.905	0.955	0.664	−0.175
11	3.069	1.168	0.790	0.658	−0.170	3.064	1.193	0.797	0.697	−0.205
12	3.071	1.154	0.787	0.658	−0.170	3.074	1.213	0.802	0.662	−0.127

[a]Bond length (Å), local mode force constant (mdyn/A), bond strength order BSO n, electron density ρ_b (e/Å³), and energy density at bond critical point H_b (Har/Å³).
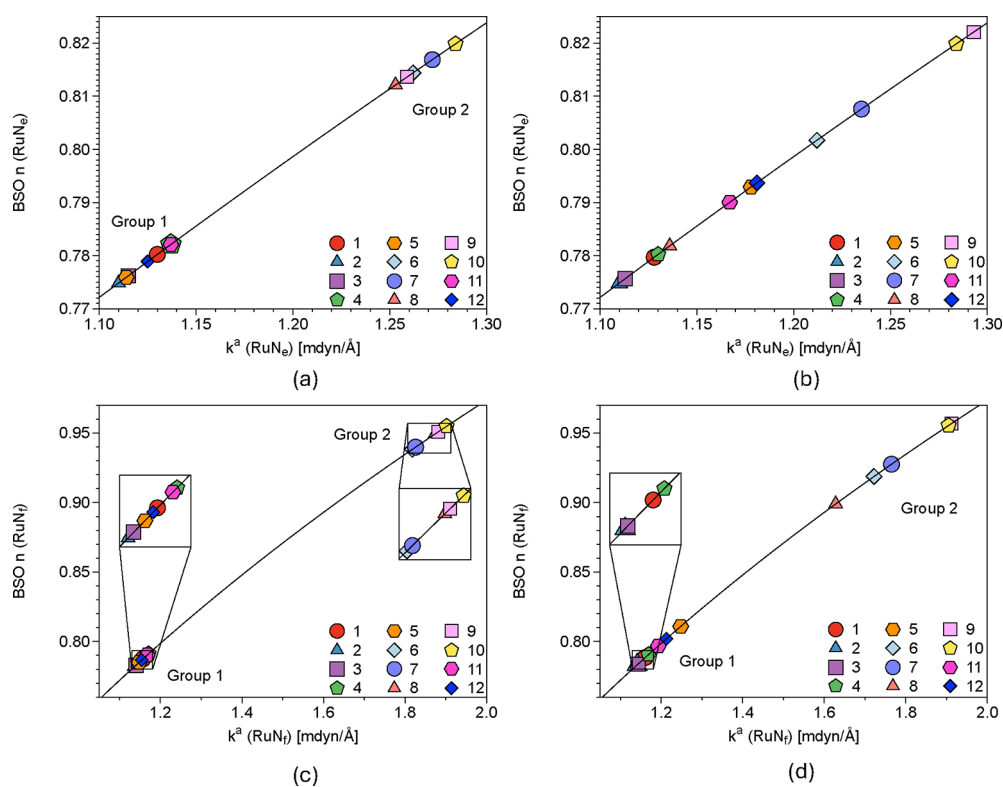

Figure 9. BSO n as a function of local mode force constant k^a for RuN bonds in PCM: (a) RuN$_e$ singlet state; (b) RuN$_e$ triplet state; (c) RuN$_f$ singlet state; (d) RuN$_f$ triplet state.
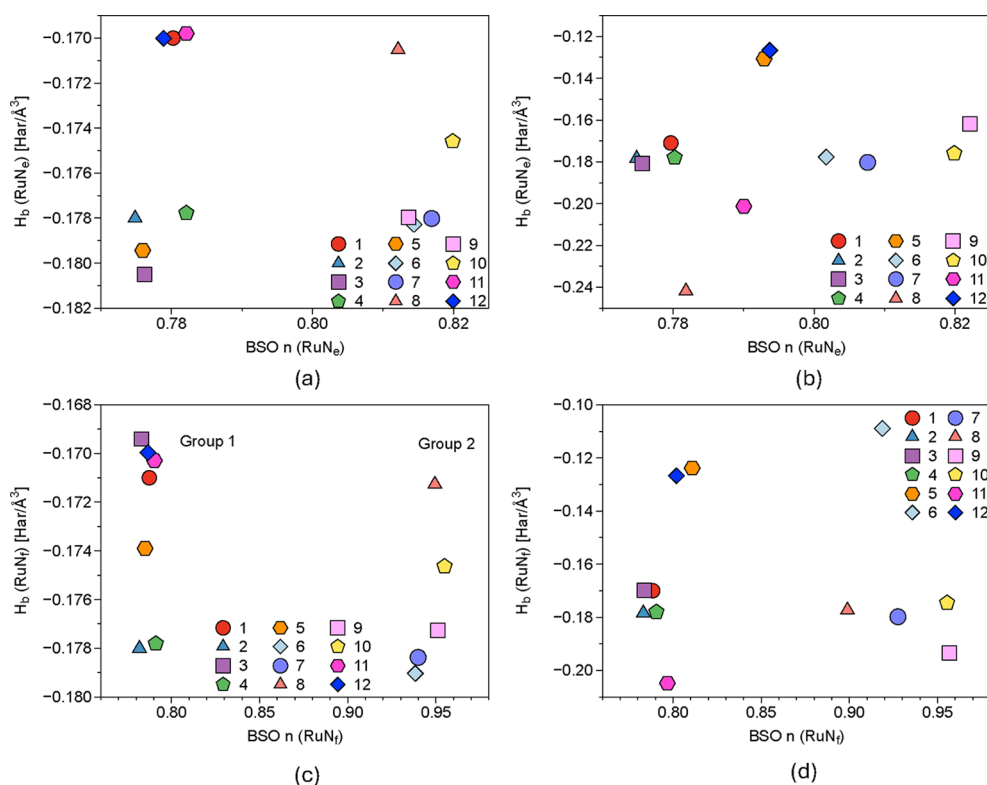
Figure 10. Relation between energy density at a bond critical point H_b and BSO n for RuN bonds in PCM: (a) RuN_e singlet state; (b) RuN_e triplet state; (c) RuN_f singlet state; (d) RuN_f triplet state.

distribution of electron density, despite identical bond strength orders. The overlap observed in the LMA parameters is evident in the QTAIM analysis of the RuN_c bond, as depicted in Figure 8c,d, with similar H_b spanning various bond strength orders in the former and similar H_b spanning similar bond strength orders in the latter. This aligns with the expected structural shift for molecules in distinct electronic states, suggesting that the disparity shown in the LMA parameters of the RuN_c bond in the triplet excited state can be largely attributed to solvent effects not always captured by QTAIM analysis. Notable outliers in the triplet state include **5**, **8**, and **12**, with **8** and **12** sharing phen ASL and exhibiting notable differences in H_b. Complexes **5** and **12** show similar H_b despite having distinct MSL and ASL.

In summary, solvation notably influences the relative ordering of bond strengths among the complexes and their H_b; it does not significantly alter the relative bond strengths compared to their gas phase geometries. This suggests a positive impact of polar solvent environments on the strength of the RuN bonds, where these effects may not be entirely reflected in changes to the energy density at the bond critical points. Notably, **1–5**, **11**, and **12** exhibit greater interaction strengths with their RuN bonds compared to **6–10**.

RuN_e and RuN_f Bonds in Solution. LMA and QTAIM parameters were similarly determined for the RuN_e and RuN_f bonds in PCM, as shown in Table 4. Conversely, these parameters display a noted decrease in the bond strengths of the RuN_e and RuN_f bonds compared to their gas-phase counterparts, likely influenced by solvochromatic effects. These interactions display notable similarity in their H_b values with differing LMA parameters, illustrating significant overlap in their QTAIM parameters not uniquely described by their LMA parameters. This trend is observed in both singlet and triplet

states coupled with similar LMA parameters in both electronic states.

To gain insight into the distinguishing features provided by the LMA parameters, Figure 9 displays the functional dependence of the BSO n values on the k^a values of the RuN_e and RuN_f bonds in PCM. Figure 9a,b depict the LMA parameters inscribed by the RuN_e bond in PCM, where Groups 1 and 2 can similarly be found in the singlet state. This further emphasizes the structural similarities of these complexes in their singlet state geometries and corresponding local modes, regardless of solvent environment. Similar disparities in this distinction can be noted for the RuN_e bond in comparing the PCM frequencies to those of the gas phase frequencies and their associated LMA parameters, as the groups intermix in the triplet state.

A greater distinction can be observed for the parameters visualized for the RuN_f bond in PCM in the singlet and triplet states shown in Figure 9c,d, where Groups 1 and 2 are observed in both electronic states. This further justifies the power of the RuN_f bond to distinguish the effects of varying MSLs and ASLs in different solvent environments, with a greater distinction of Group 2 in the triplet state compared with its gas phase counterpart. A similar trend can be noted for RuN_b and RuN_c bonds toward RuN_e and RuN_f bonds as previously described for their gas phase systems. Where the bond strengths of Group 1 are lower for their RuN_e and RuN_f bonds, these values are higher for their RuN_b and RuN_c bonds. Where the bond strengths of Group 2 are higher for their RuN_e and RuN_f bonds, these values are lower for their RuN_b and RuN_c bonds. We will shift to describe the relatedness of these LMA parameters with those of their QTAIM parameters.

The relationship between the QTAIM parameter H_b and the LMA parameter BSO n is shown in Figure 10 for the RuN_e and

RuN_f bonds in the complexes' singlet and triplet states. Figure 10a,b display this correspondence for the RuN_e bond in the singlet and triplet states, where the energy density does not well describe the trends observed in the LMA parameters for this bond in PCM. The covalent nature of these bonds does not directly impact the strength of these bonds, where all bonds show varying degrees of covalency for similar bond strengths.

While Groups 1 and 2 could be observed in the singlet state, the extent of variation spanning these two subsets does not sponsor an official grouping according to our analysis. In Figure 10c,d, the RuN_f bond preserves the trend observed with its prior gas phase counterparts regarding their bond strength, yet these bonds span nearly identical measures of covalency in the singlet state, and more varying measures of covalency in the triplet state. While all interactions in this study are notably covalent by the Cremer-Kraka criterion, the extent of covalency spanning different ASLs and MSLs is not well described by the RuN_f bond alone in the PCM environment. While these trends can be distinguished through the LMA perspective of RuN_f bonds and their direct effects on RuN_b, RuN_c, and RuN_e bonds, determining their covalency does not unravel unique information about coordinating effects of bond strengths on these systems.

Similar trends are observed in characterizing the LMA parameters of RuN_e and RuN_f bonds with regards to their gas phase counterparts and PCM parameters of RuN_c and RuN_d bonds, yet, molecular systems can often time introduce additional complexity which can skew the relative contributions of covalent character in describing the strength of these interactions in implicit solvent systems. While modeling solvation in chemical systems offers the benefits of modeling chemical effects in biologically relevant systems, the power of LMA persists in characterizing the extent of substitution effects and ligand modifications on chemical systems, namely, those of Ru(II) polypyridyl complexes.

Nonbonded $\pi-\pi$ Stacking Interaction between MSL and DNA. Table 5 shows LMA parameters of the nonbonded interaction between selected aromatic rings of MSL and DNA base nucleobase Adenine, such as the interaction length q_n and the local mode force constant k^a, obtained from QM/MM calculations. This table involves the selected Ru complexes investigated in this study (**1**, **2**, **3**, and **11**), which are the

Table 5. Parameters of Nonbonded Interactions between Selected Aromatic Rings of MSL and Adenine in DNA[a]

complex	$q_n(O_A-O_B)$	$k^a(O_A-O_B)$	ΔE
		singlet	
1	3.195	0.399	34.655
2	3.264	0.200	50.544
3	3.362	0.260	52.085
11	3.176	0.324	49.781
		triplet	
1	3.225	0.286	
2	3.383	0.221	
3	3.385	0.231	
11	3.232	0.322	

[a]Nonbonded interaction length for the local mode $q_n(O_A-O_B)$ (Å), local mode force constant $k^a(O_A-O_B)$ (mdyn/A), singlet–triplet energy difference ΔE (kcal/mol), for singlet and triplet electronic states of complexes **1**, **2**, **3**, and **11**.

simplest modifications of MSL and ASL in the primary Ru-complex **1**. The interaction between the aromatic rings of MSL and the DNA nucleobase Adenine is specified in Figure 2. Table 5 also includes the splitting energy (ΔE) between the singlet and triplet electronic states for the complexes in DNA. According to this table, the strongest interaction between MSL and Adenine in the singlet state is observed for **1** (0.399 mdyn/Å), which also shows the smallest ΔE (34.655 kcal/mol). However, In the triplet electronic state, the strongest interaction is observed for **11** (0.322 mdyn/A), which displays the second smallest ΔE in the series (49.781 kcal/mol). This suggests that the phen ASL in **1**, with extended π-conjugation compared to the bpy ASL in **2** and dmb ASL in **3**, strengthens the interaction between MSL and Adenine in **1**. The greater aromaticity and electronic delocalization of the phen ring contribute to a smaller ΔE, facilitating a more favorable ST transition.[75-77]

In **11**, where the MSL is modified via terminal nitrile substitution, a slight decrease in the $q_n(O_A-O_B)$ interaction length local mode and $k^a(O_A-O_B)$ is observed, accompanied by a higher ΔE. This suggests a less favorable nonbonded interaction with Adenine in the singlet state and a greater ΔE for a ST transition. However, in the triplet state, **11** displays a larger $k^a(O_A-O_B)$ than **1**, implying a more favorable nonbonded interaction in DNA upon excitation.

Considering the accessibility of the ^{3}MLCT state, **11** presents a greater barrier toward phosphorescence, but a more favorable interaction in the triplet state. This suggests it could still be a viable candidate for photochemotherapy, offering a more favorable nonbonded interaction in its triplet state comparatively to **1**. However, **1** exhibits a greater interaction strength with the nucleobase Adenine in the singlet state, characterized by a lower ΔE. Thus, there exists a trade-off between energetics and interaction strength. For a more favorable phosphorescence, i.e., generation of ROS, extended nonsubstituted π-conjugated systems would be recommended as photoactive DNA intercalators. For stronger stacking interaction post photoexcitation, adding electron-withdrawing groups to the terminal ends of the MSL of extended π-conjugated systems is advisable for a more localized ROS generation. It is important to note that characterizing the excited state dynamics of these complexes involves excitation from the singlet ground state to a ^{1}MLCT state, followed by an intersystem crossing to a ^{3}MLCT state, which then phosphoresces back to the singlet ground state.[78] Yet this analysis still offers insight into the relative ability of these complexes to both efficiently stack in DNA and participate in photochemical events.

CONCLUSION

Our investigation has provided valuable insights into the electronic properties of RuN bonds Ru(II) polypyridyl complexes. Characterizing the central RuN bond strengths, in the gas phase and solution, has shed light on the complexes' electronic structure in different environments and the extent to which solvation impacts chemical bond strengths. Furthermore, the QM/MM approach has enabled a quantitative analysis of the nonbonded interaction strengths between MSL and DNA nucleobases, highlighting the potential of these complexes as DNA intercalators.

Based on the results obtained from our calculations, we recommend **1** and **11** for additional investigations in this regard, as both show viable interaction strengths with the

nucleobase Adenine in AT/TA gaps of DNA, with suitable motifs such as TATA boxes and promoter regions.[79,80] Complex **1** displays a smaller ΔE and a greater $k^a(O_A-O_B)$ in its singlet state, suggesting a more favorable photoexcitation, but a potentially weaker interaction with a ^{3}MLCT state. Conversely, **11** exhibits a larger ΔE and a greater $k^a(O_A-O_B)$ in its triplet state, indicating a less favorable photoinduced transition but a stronger interaction with DNA nucleobases post-excitation. We hope our study inspires future experimental and computational work in designing novel polypyridyl complexes and that our new quantitative measure of $\pi-\pi$ stacking interactions in DNA will find general application in the field.

ASSOCIATED CONTENT

Supporting Information

The Supporting Information is available free of charge at https://pubs.acs.org/doi/10.1021/acs.jpca.4c02954.

Data for RuN$_a$ and RuN$_d$ bonds, NBO charges, and Cartesian coordinates for all 12 complexes in their singlet and triplet states, gas phase and solution, and the QM/MM data for complexes **1**, **2**, **3**, and **11** (ZIP)

AUTHOR INFORMATION

Corresponding Author

Elfi Kraka − *Computational and Theoretical Chemistry Group (CATCO), Department of Chemistry, Southern Methodist University, Dallas, Texas 75275-0314, United States;* orcid.org/0000-0002-9658-5626; Email: ekraka@gmail.com

Authors

Hunter La Force − *Computational and Theoretical Chemistry Group (CATCO), Department of Chemistry, Southern Methodist University, Dallas, Texas 75275-0314, United States*

Marek Freindorf − *Computational and Theoretical Chemistry Group (CATCO), Department of Chemistry, Southern Methodist University, Dallas, Texas 75275-0314, United States*

Complete contact information is available at:
https://pubs.acs.org/10.1021/acs.jpca.4c02954

Notes

The authors declare no competing financial interest.

ACKNOWLEDGMENTS

REFERENCES

(1) Karges, J.; Stokes, R. W.; Cohen, S. M. Metal complexes for therapeutic applications. *Trends Chem.* **2021**, *3*, 523−534.

(2) Zhang, P.; Sadler, P. J. Advances in the design of organometallic anticancer complexes. *J. Organomet. Chem.* **2017**, *839*, 5−14.

(3) Rosenberg, B. Cisplatin: Its history and possible mechanisms of action. *Cisplatin*; Elsevier, 1980; pp 9−20.

(4) Zamble, D. B.; Lippard, S. J. Cisplatin and DNA repair in cancer chemotherapy. *Trends Biochem. Sci.* **1995**, *20*, 435−439.

(5) Aldossary, S. A. Review on Pharmacology of Cisplatin: Clinical Use, Toxicity and Mechanism of Resistance of Cisplatin. *Biomed. Pharmaco. J.* **2019**, *12*, 7−15.

(6) Lee, S. Y.; Kim, C. Y.; Nam, T.-G. Ruthenium Complexes as Anticancer Agents: A Brief History and Perspectives. *Drug. Des. Devel. Ther.* **2020**, *14*, 5375−5392.

(7) Rademaker-Lakhai, J. M.; van den Bongard, D.; Pluim, D.; Beijnen, J. H.; Schellens, J. H. M. A Phase I and Pharmacological Study with Imidazolium-trans-DMSO-imidazole-tetrachlororuthenate, a Novel Ruthenium Anticancer Agent. *Clin. Cancer Res.* **2004**, *10*, 3717−3727.

(8) Alessio, E. Thirty years of the drug candidate NAMI-A and the myths in the field of ruthenium anticancer compounds: a personal perspective. *Eur. J. Inorg. Chem.* **2017**, *2017*, 1549−1560.

(9) Trondl, R.; Heffeter, P.; Kowol, C. R.; Jakupec, M. A.; Berger, W.; Keppler, B. K. NKP-1339, the first ruthenium-based anticancer drug on the edge to clinical application. *Chem. Sci.* **2014**, *5*, 2925−2932.

(10) Hartinger, C.; Jakupec, M.; Zorbas-Seifried, S.; Groessl, M.; Egger, A.; Berger, W.; Zorbas, H.; Dyson, P.; Keppler, B. KP1019, A New Redox-Active Anticancer Agent − Preclinical Development and Results of a Clinical Phase I Study in Tumor Patients. *Chem. Biodivers.* **2008**, *5*, 2140−2155.

(11) Monro, S.; Colón, K. L.; Yin, H.; Roque, J. I.; Konda, P.; Gujar, S.; Thummel, R. P.; Lilge, L.; Cameron, C. G.; McFarland, S. A. Transition Metal Complexes and Photodynamic Therapy from a Tumor-Centered Approach: Challenges, Opportunities, and Highlights from the Development of TLD1433. *Chem. Rev.* **2019**, *119*, 797−828.

(12) Sonkar, C.; Sarkar, S.; Mukhopadhyay, S. Ruthenium (II)−arene complexes as anti-metastatic agents, and related techniques. *RSC Med. Chem.* **2022**, *13*, 22−38.

(13) Swaminathan, S.; Karvembu, R. Dichloro Ru (II)-p-cymene-1, 3, 5-triaza-7-phosphaadamantane (RAPTA-C): A case study. *ACS Pharmacol. Transl. Sci.* **2023**, *6*, 982−996.

(14) Hongthong, K.; Nhukeaw, T.; Temboot, P.; Dyson, P. J.; Ratanaphan, A. Anticancer activity of RAPTA-EA1 in triple-negative BRCA1 proficient breast cancer cells: single and combined treatment with the PARP inhibitor olaparib. *Heliyon* **2021**, *7*, e07749.

(15) Shum, J.; Leung, P. K.-K.; Lo, K. K.-W. Luminescent Ruthenium(II) Polypyridine Complexes for a Wide Variety of Biomolecular and Cellular Applications. *Inorg. Chem.* **2019**, *58*, 2231−2247.

(16) Cerfontaine, S.; Troian-Gautier, L.; Duez, Q.; Cornil, J.; Gerbaux, P.; Elias, B. MLCT excited-state behavior of trinuclear ruthenium (II) 2, 2′-bipyridine complexes. *Inorg. Chem.* **2021**, *60*, 366−379.

(17) Raza, A.; Archer, S. A.; Fairbanks, S. D.; Smitten, K. L.; Botchway, S. W.; Thomas, J. A.; MacNeil, S.; Haycock, J. W. A dinuclear ruthenium (II) complex excited by near-infrared light through two-photon absorption induces phototoxicity deep within hypoxic regions of melanoma cancer spheroids. *J. Am. Chem. Soc.* **2020**, *142*, 4639−4647.

(18) Graham, K.; Unger, E. Overcoming tumor hypoxia as a barrier to radiotherapy, chemotherapy and immunotherapy in cancer treatment. *Int. J. Nanomed.* **2018**, *13*, 6049−6058.

(19) Wei, F.; Kuang, S.; Rees, T. W.; Liao, X.; Liu, J.; Luo, D.; Wang, J.; Zhang, X.; Ji, L.; Chao, H. Ruthenium (II) complexes coordinated to graphitic carbon nitride: oxygen self-sufficient photosensitizers which produce multiple ROS for photodynamic therapy in hypoxia. *Biomaterials* **2021**, *276*, 121064.

(20) Poynton, F. E.; Bright, S. A.; Blasco, S.; Williams, D. C.; Kelly, J. M.; Gunnlaugsson, T. The development of ruthenium (II) polypyridyl complexes and conjugates for in vitro cellular and in vivo applications. *Chem. Soc. Rev.* **2017**, *46*, 7706−7756.

(21) Mari, C.; Pierroz, V.; Ferrari, S.; Gasser, G. Combination of Ru(II) complexes and light: new frontiers in cancer therapy. *Chem. Sci.* **2015**, *6*, 2660−2686.

(22) Kondrasenko, I.; Chung, K.-y.; Chen, Y.-T.; Koivistoinen, J.; Grachova, E. V.; Karttunen, A. J.; Chou, P.-T.; Koshevoy, I. O. Harnessing fluorescence versus phosphorescence ratio via ancillary ligand fine-tuned MLCT contribution. *J. Phys. Chem. C* **2016**, *120*, 12196−12206.

(23) Son, A.; Kawasaki, A.; Hara, D.; Ito, T.; Tanabe, K. Phosphorescent ruthenium complexes with a nitroimidazole unit that image oxygen fluctuation in tumor tissue. *Eur. J. Chem.* **2015**, *21*, 2527−2536.

(24) Friedman, A. E.; Chambron, J.-C.; Sauvage, J.-P.; Turro, N. J.; Barton, J. K. Molecular '"Light Switch" for DNA: Ru(bpy)₂(dppz)²⁺. *J. Am. Chem. Soc.* **1990**, *112*, 4960−4962.

(25) Boynton, A. N.; Marcélis, L.; Barton, J. K. [Ru(Me4phen)-2dppz]2+, a Light Switch for DNA Mismatches. *J. Am. Chem. Soc.* **2016**, *138*, 5020−5023.

(26) Di Pietro, M. L.; La Ganga, G.; Nastasi, F.; Puntoriero, F. Ru (II)-dppz derivatives and their interactions with DNA: Thirty years and counting. *Appl. Sci.* **2021**, *11*, 3038.

(27) McQuaid, K.; Hall, J. P.; Brazier, J. A.; Cardin, D. J.; Cardin, C. J. X-ray Crystal Structures Show DNA Stacking Advantage of Terminal Nitrile Substitution in Ru-dppz Complexes. *Eur. J. Chem.* **2018**, *24*, 15859−15867.

(28) Deng, J.-H.; Luo, J.; Mao, Y.-L.; Lai, S.; Gong, Y.-N.; Zhong, D.-C.; Lu, T.-B. π-π stacking interactions: Non-negligible forces for stabilizing porous supramolecular frameworks. *Sci. Adv.* **2020**, *6*, eaax9976.

(29) Kraka, E.; Quintano, M.; La Force, H. W.; Antonio, J. J.; Freindorf, M. The Local Vibrational Mode Theory and Its Place in the Vibrational Spectroscopy Arena. *J. Phys. Chem. A* **2022**, *126*, 8781−8900.

(30) Kraka, E.; Zou, W.; Tao, Y. Decoding Chemical Information from Vibrational Spectroscopy Data: Local Vibrational Mode Theory. *WIREs: Comput. Mol. Sci.* **2020**, *10*, 1480.

(31) Elgar, C. E.; Yusoh, N. A.; Tiley, P. R.; Kolozsvári, N.; Bennett, L. G.; Gamble, A.; Péan, E. V.; Davies, M. L.; Staples, C. J.; Ahmad, H.; et al. Ruthenium (II) polypyridyl complexes as FRET donors: structure-and sequence-selective DNA-binding and anticancer properties. *J. Am. Chem. Soc.* **2023**, *145*, 1236−1246.

(32) Miao, Q.; Xu, Y.; Miao, T.; Xu, L. Theoretical insights and design of Ru (II)-based complexes with DNA-photocleavage properties. *J. Indian Chem. Soc.* **2022**, *99*, 100320.

(33) Niyazi, H.; Hall, J. P.; O'sullivan, K.; Winter, G.; Sorensen, T.; Kelly, J. M.; Cardin, C. J. Crystal structures of Λ-[Ru (phen) 2dppz] 2+ with oligonucleotides containing TA/TA and AT/AT steps show two intercalation modes. *Nat. Chem.* **2012**, *4*, 621−628.

(34) Mardirossian, N.; Head-Gordon, M. Thirty years of density functional theory in computational chemistry: An overview and extensive assessment of 200 density functionals. *Mol. Phys.* **2017**, *115*, 2315−2372.

(35) Dunning, T. H., Jr Gaussian basis sets for use in correlated molecular calculations. I. The atoms boron through neon and hydrogen. *J. Chem. Phys.* **1989**, *90*, 1007−1023.

(36) Kendall, R. A.; Dunning, T. H.; Harrison, R. J. Electron affinities for the first-row atoms revisited. Systematic basis sets and wave functions. *J. Chem. Phys.* **1992**, *96*, 6796−6806.

(37) Adamo, C.; Barone, V. Toward reliable density functional methods without adjustable parameters: The PBE0 model. *Chem. Phys.* **1999**, *110*, 6158−6170.

(38) Li, G.; Chen, L.; Wang, X.; Wu, L.; Jie, X.; Chen, J. Electronic Structures, DNA-binding, SAR, and Spectral Properties of Ruthenium Methylimidazole Complexes [Ru(MeIm)₄L]²⁺ (L = iip, tip, 2ntz). *Chin. J. Chem. Phys.* **2014**, *27*, 159−167.

(39) McCutcheon, M.; Freindorf, M.; Kraka, E. Bonding in Nitrile Photo−dissociating Ruthenium Drug Candidates - A Local Vibrational Mode Study. *J. Chem. Phys.* **2022**, *157*, 014301-1−014301-15.

(40) La Force, H.; Kraka, E. Characterizing guanine's binding modes with potential Ru(II) monofunctional adducts: A local vibrational mode study. *Chem. Phys. Lett.* **2023**, *828*, 140733.

(41) Adamo, C.; Scuseria, G. E.; Barone, V. Accurate excitation energies from time-dependent density functional theory: Assessing the PBE0 model. *J. Chem. Phys.* **1999**, *111*, 2889−2899.

(42) Garza, A. J.; Scuseria, G. E.; Ruzsinszky, A.; Sun, J.; Perdew, J. P. The two pillars: density and spin-density functional theories. *Mol. Phys.* **2016**, *114*, 928−931.

(43) Tsuzuki, S.; Uchimaru, T. Accuracy of intermolecular interaction energies, particularly those of hetero-atom containing molecules obtained by DFT calculations with Grimme's D2, D3 and D3BJ dispersion corrections. *Phys. Chem. Chem. Phys.* **2020**, *22*, 22508−22519.

(44) Fuentealba, P.; Preuss, H.; Stoll, H.; Von Szentpály, L. A proper account of core-polarization with pseudopotentials: single valence-electron alkali compounds. *Chem. Phys. Lett.* **1982**, *89*, 418−422.

(45) Andrae, D.; Haeussermann, U.; Dolg, M.; Stoll, H.; Preuss, H. Energy-adjusted ab initio pseudopotentials for the second and third row transition elements. *Theor. Chim. Act.* **1990**, *77*, 123−141.

(46) Tarakeshwar, P.; Kim, K. S.; Kraka, E.; Cremer, D. Structure and Stability of Fluorine-Substituted Benzene-Argon Complexes: The Decisive Role of Exchange-Repulsion and Dispersion Interactions. *J. Chem. Phys.* **2001**, *115*, 6018−6029.

(47) Tomasi, J.; Mennucci, B.; Cammi, R. Quantum mechanical continuum solvation models. *Chem. Rev.* **2005**, *105*, 2999−3094.

(48) Gräfenstein, J.; Cremer, D. Efficient DFT integrations by locally augmented radial grids. *J. Chem. Phys.* **2007**, *127*, 164113.

(49) van der Kamp, M. W.; Mulholland, A. J. Combined Quantum Mechanics/Molecular Mechanics (QM/MM) Methods in Computational Enzymology. *Biochemistry* **2013**, *52*, 2708−2728.

(50) Tzeliou, C. E.; Mermigki, M. A.; Tzeli, D. Review on the QM/MM Methodologies and Their Application to Metalloproteins. *Molecules* **2022**, *27*, 2660.

(51) Warshel, A.; Karplus, M. Calculation of ground and excited state potential surfaces of conjugated molecules. I. Formulation and parametrization. *J. Am. Chem. Soc.* **1972**, *94*, 5612−5625.

(52) Warshel, A.; Levitt, M. Theoretical studies of enzymic reactions: Dielectric, electrostatic and steric stabilization of the carbonium ion in the reaction of lysozyme. *J. Mol. Biol.* **1976**, *103*, 227−249.

(53) Frisch, M. J.; Trucks, G. W.; Schlegel, H. B.; Scuseria, G. E.; Robb, M. A.; Cheeseman, J. R.; Scalmani, G.; Barone, V.; Petersson, G. A.; Nakatsuji, H.; et al. *Gaussian 16*, Revision C.01; Gaussian Inc.: Wallingford, CT, 2016.

(54) Li, P.; Merz, K. M. *MCPB.py*, A python based metal center parameter builder; 2016.

(55) Jorgensen, W. L.; Chandrasekhar, J.; Madura, J. D.; Impey, R. W.; Klein, M. L. Comparison of simple potential functions for simulating liquid water. *J. Chem. Phys.* **1983**, *79*, 926−935.

(56) Case, D.; Aktulga, H.; Belfon, K.; Ben-Shalom, I.; Berryman, J.; Brozell, S.; Cerutti, D.; T.E. Cheatham, I.; Cisneros, G.; Cruzeiro, V.; et al. *Amber 2022*; University of California: San Francisco, 2022.

(57) Dapprich, S.; Komáromi, I.; Byun, K. S.; Morokuma, K.; Frisch, M. J. A new ONIOM implementation in Gaussian98. Part I. The calculation of energies, gradients, vibrational frequencies and electric field derivatives. *J. Mol. Struct.: THEOCHEM* **1999**, *461*, 1−21.

(58) Wilson, E. B.; Decius, J. C.; Cross, P. C. *Molecular Vibrations: the Theory of Infrared and Raman Vibrational Spectra*; McGraw-Hill, New York, 1955; pp 59−136.

(59) Verma, N.; Tao, Y.; Zou, W.; Chen, X.; Chen, X.; Freindorf, M.; Kraka, E. A Critical Evaluation of Vibrational Stark Effect (VSE) Probes with the Local Vibrational Mode Theory. *Sensors* **2020**, *20*, 2358.

(60) Zou, W.; Cremer, D. C₂ in a Box: Determining its Intrinsic Bond Strength for the X¹Σ⁺_g Ground State. *Chem.—Eur. J.* **2016**, *22*, 4087−4097.

(61) Kraka, E.; Larsson, J. A.; Cremer, D. Generalization of the Badger Rule Based on the Use of Adiabatic Vibrational Modes. In *Computational Spectroscopy*; Grunenberg, J., Ed.; Wiley: New York, 2010; pp 105−149.

(62) Bridgeman, A. J.; Cavigliasso, G.; Ireland, L. R.; Rothery, J. The Mayer bond order as a tool in chemistry. *J. Chem. Soc., Dalton Trans.* **2001**, 2095−2108.

(63) Cremer, D.; Kraka, E. Chemical Bonds without Bonding Electron Density? Does the Difference Electron-Density Analysis Suffice for a Description of the Chemical Bond? *Angew. Chem., Int. Ed.* **1984**, *23*, 627−628.

(64) Cremer, D.; Kraka, E. A Description of the Chemical Bond in Terms of Local Properties of Electron Density and Energy. *Croatica Chem. Acta* **1984**, *57*, 1259−1281.

(65) Bader, R. F. W. *Atoms in Molecules: A Quantum Theory*; International Series of Monographs on Chemistry; Clarendon Press, 1994.

(66) Popelier, P. L. *Atoms in Molecules: An Introduction*; Prentice Hall, 2000.

(67) Zou, W.; Moura, R., Jr.; Quintano, M.; Bodo, F.; Tao, Y.; Freindorf, M.; Makoś, M. Z.; Verma, N.; Cremer, D.; Kraka, E. *LModeA2023. Computational and Theoretical Chemistry Group (CATCO)*; Southern Methodist University: Dallas, TX, USA, 2023.

(68) Keith, T. A. *AIMAll*, Version 19.10.12; TK Gristmill Software, Overland Park KS, USA, 2019. aim.tkgristmill.com.

(69) Reed, A. E.; Curtiss, L. A.; Weinhold, F. Intermolecular Interactions from a Natural Bond Orbital, Donor-Acceptor Viewpoint. *Chem. Rev.* **1988**, *88*, 899−926.

(70) Weinhold, F.; Landis, C. R. *Valency and Bonding: A Natural Bond Orbital Donor-Acceptor Perspective*; Cambridge University Press, 2005.

(71) Glendening, E. D.; Badenhoop, J. K.; Reed, A. E.; Carpenter, J. E.; Bohmann, J. A.; Morales, C. M.; Landis, C. R.; Weinhold, F. *NBO6*; Theoretical Chemistry Institute, University of Wisconsin-Madison, 2013.

(72) Zwickel, A.; Creutz, C. Charge-transfer spectra of ruthenium (II) complexes. *Inorg. Chem.* **1971**, *10*, 2395−2399.

(73) Toledo, J. C.; dos Santos Lima Neto, B.; Franco, D. W. Mutual effects in the chemical properties of the ruthenium metal center and ancillary ligands upon coordination. *Coord. Chem. Rev.* **2005**, *249*, 419−431.

(74) Gawelda, W.; Johnson, M.; de Groot, F. M.; Abela, R.; Bressler, C.; Chergui, M. Electronic and molecular structure of photoexcited [RuII (bpy) 3] 2+ probed by picosecond X-ray absorption spectroscopy. *J. Am. Chem. Soc.* **2006**, *128*, 5001−5009.

(75) Makedonas, C.; Mitsopoulou, C. A. The Relationship Between Aromaticity and Charge-Transfer Transitions: A Combined Study of Square-Planar Metal Complexes Based on DFT, NMR and Nucleus-Independent Chemical Shifts. *Eur. J. Inorg. Chem.* **2006**, *2006*, 2460−2468.

(76) Feixas, F.; Matito, E.; Poater, J.; Solà, M. Quantifying aromaticity with electron delocalisation measures. *Chem. Soc. Rev.* **2015**, *44*, 6434−6451.

(77) Oh, J.; Sung, Y. M.; Mori, H.; Park, S.; Jorner, K.; Ottosson, H.; Lim, M.; Osuka, A.; Kim, D. Unraveling excited-singlet-state aromaticity via vibrational analysis. *Chem.* **2017**, *3*, 870−880.

(78) Balzani, V.; Ceroni, P.; Juris, A. *Photochemistry and photophysics: concepts, research, applications*; John Wiley & Sons, 2014.

(79) Mishal, R.; Luna-Arias, J. P. Role of the TATA-box binding protein (TBP) and associated family members in transcription regulation. *Gene* **2022**, *833*, 146581.

(80) Levy, S.; Somasundaram, L.; Raj, I. X.; Ic-Mex, D.; Phal, A.; Schmidt, S.; Ng, W. I.; Mar, D.; Decarreau, J.; Moss, N.; et al. dCas9 fusion to computer-designed PRC2 inhibitor reveals functional TATA box in distal promoter region. *Cell Rep.* **2022**, *38*, 110457.